RSC Advances

PAPER

View Article Online
View Journal | View Issue

Cite this: *RSC Adv.*, 2025, **15**, 37511

Photo-detection evaluation of an *n*-WO_3/p-Si heterostructure for visible wavelength detection

Yasir Jaafar Jameel,[a] Alaa Abdulhameed Abdulmajeed,[b] Asaad Shakir Hussein,[c] Ethar Yahya Salih *[d] and Maryam Abdulghafoor Ahmed[d]

Received 13th August 2025
Accepted 23rd September 2025

DOI: 10.1039/d5ra05971b

rsc.li/rsc-advances

This article demonstrates a detailed fabrication procedure for a visible light n-type WO_3/p-type Si photodetector as a function of laser fluence. The microstructural characteristics of the deposited WO_3 layer/s, using pulsed laser deposition, were systematically investigated. The attained optical band gap revealed an average value of 2.6 eV, while the morphological features attained an increased nanoparticle diameter from 36.9 to 43.9 nm for fluences of 4.46 and 7.01 J cm^{-2}, respectively. Further, opto-electrical evaluation demonstrated a wavelength-dependent profile with the highest photo-responsivity (R_λ) value of 0.87 A W^{-1} at 460 nm and 15.3 μW cm^{-2}, and a photo-detectivity (D^*) and external quantum efficiency (EQE) of 7.4 $\times 10^{11}$ Jones and 307%, respectively, were achieved. The dependency on illumination power suggested a positive correlation between the incident light intensity increment and the addressed figures of merit. In detail, R_λ and D^* values increased up to 1.09 A W^{-1} and 9.3 $\times 10^{11}$ Jones under an illumination of 57.1 μW cm^{-2} at 460 nm, with an average R^2 value of 0.899. The time-resolved characteristics demonstrated steady photodetector performance with considerable response/recovery times of 163 and 172 ms, respectively.

1. Introduction

Silicon (Si)-based optoelectronics technology, with increased opto-electrical performance, has been widely examined for practical applications, such as environmental and biological research, flame detection, military UV/Vis/IR monitoring and communication.[1–3] However, the development of technologies for detection in the visible region, particularly photodetectors, requires continuous advancement, combining high sensitivity (responsivity, detectivity, light-to-dark ratio, and external quantum efficiency) with pronounced time-resolved characteristics, especially fast response.[4–7] Particularly, there are two main binary detection pathways, the so-called photo-conductive and photo-voltaic modes; the latter typically includes homo-, hetero-, and Schottky junction photodetectors. The photo-voltaic mode, particularly homo/heterojunctions, brings about higher performance as compared to the photo-conductive mode, due to the exceptionally fast-response and high sensitivity characteristics. In this context, a number of semiconductor materials have been given due consideration to enhance the addressed figures of merit, such as cadmium oxide (CdO), copper oxide (CuO), cadmium sulfide (CdS), cadmium telluride (CdTe), and cadmium selenide (CdSe).[8–14] WO_3, which is an intrinsic n-type semiconductor oxide material, demonstrates an indirect visible light absorption edge around 440–516 nm, with high temperature resistance and chemical stability. WO_3 also displays non-stoichiometric features, through which a substantial amount of oxygen vacancies can be accommodated. Structurally, WO_3 exhibits a distorted cubic perovskite-like arrangement, where oxygen atoms occupy the corners of the unit cell, while tungsten atoms reside at the center of the surrounding octahedra.[15–19] Herein, we present a procedure for the fabrication of an n-type WO_3/p-type Si heterostructure for optoelectronic application, particularly a visible light photodetector. In detail, WO_3 was deposited onto a p-type Si substrate through the PLD technique, using different laser fluences. Furthermore, a robust correlation between the microstructural features and the opto-electronics characteristics was established.

2. Methodology

Mechanically hard-pressed WO_3 powder (99.995%, n-type, Sigma-Aldrich) was deposited on a multi-cycled, cleaned p-type Si wafer (Sigma-Aldrich, 540 μm, single-side polished) with dimensions of 1 cm^2. WO_3 target was positioned vertically at a distance of 5 cm from the utilized p-type Si wafer, after which a 532 nm ND-YAG laser was focused on the WO_3 target at an angle of 45° for 900 pulses, with a pulse width of 10 ns and a repetition frequency of 6 Hz (Fig. 1). The laser fluence was

[a]Dewan Alwaqf Al-Sunni, The Financial and Administrative Office, Baghdad, Iraq
[b]Ministry of Education, Direction of Education in Al-Rasafa, Baghdad, Iraq
[c]Department of Medical Physics, Al-Taff University College, Karbala, Iraq
[d]College of Energy and Environmental Sciences, Al-Karkh University of Science, Baghdad 10081, Iraq. E-mail: ethar988@gmail.com; ethar@kus.edu.iq

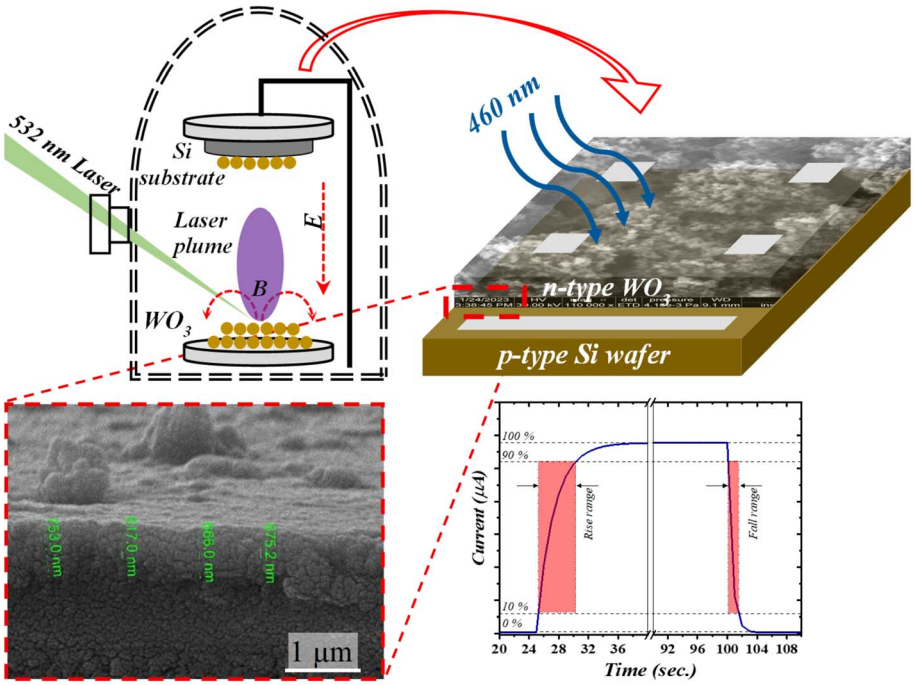

Fig. 1 Schematic representation of the fabricated device and deposition process; the inset shows the thickness of the deposited WO_3 layer.

varied to obtain WO_3 layer modification (4.46, 5.37, and 7.01 J cm^{-2}); the spot size and laser fluence were estimated using a spot-sensitive paper and laser power meter, respectively. Finally, a complete photodetector geometry was accomplished through Ag metal contacts (0.1 cm^2) on the top of both the Si wafer and WO_3 layer using a thermal evaporation approach. A schematic illustration of the fabricated photodetector is depicted in Fig. 1, with the optimum layer having an average thickness of 678 nm, as shown in the inset. The deposited layers' structural features were investigated using Fourier transform infrared spectroscopy (FT-IR, ALPHA-II Bruker) and X-ray diffraction (XRD, SHIMADZU). The morphological properties were determined using a field emission scanning electron microscope (FE-SEM, JRM-7601F), and the optical characteristics were investigated using photoluminescence (PL, LS-51) and ultraviolet visible light (UV-Vis, SHIMADZU) approaches. Finally, the fabricated devices were evaluated through a lab-based setup consisting of a SMU Keithley 2402 with a light source that goes through multiple bandpass filters (375–720 nm). The time-resolved features were considered from 10% to 90% of the total attained current under multiple on/off light states, as elucidated in Fig. 1.

3. Results and discussion

3.1 Deposited layers characteristics

Fig. 2(a) depicts the XRD patterns of the deposited WO_3 layers obtained by using different laser fluence values. In particular, angles acquired at around 23.04°, 23.6°, 24.2°, 26.56°, 33.28°, 33.88°, 51.76°, and 58.88° correspond to the (002), (020), (200), (112), (022), (202), (400), and (420) planes, respectively; this in turn suggests the occurrence of a naturally formed polycrystalline structure of WO_3 in conjunction with the JCPDS data card no. 42-1034. It is worth mentioning that the plane attained at 33.28° (022) was not found under a laser fluence of 4.46 J cm^{-2}, which could be due to low laser energy resulting in lower structural formation.

Fig. 2(b) illustrates the FT-IR spectra, which consist of two different peaks at around 3450 cm^{-1} and 1625 cm^{-1}; these are attributed to the intercalated H_2O molecules and WO_3 symmetric stretching vibrations, and the adsorbed water (H–O–H) bond deformation vibrations, respectively. Two other peaks attained at 821 cm^{-1} and 769 cm^{-1} resulted from the O–W–O bond stretching in WO_3.[20]

The optical absorbance exhibited a cut-off phenomenon ranging from 350 nm to 450 nm, while the optical bandgap was determined using the Tauc relation.[12] The inset in Fig. 2(c) shows optical bandgap values of 2.69, 2.71, and 2.74 eV for the utilized laser fluences of 4.46, 5.37, and 7.01 J cm^{-2}, respectively.

The deposited WO_3 film topography (Fig. 2(d–f)) with different laser fluences revealed compact surface features. A higher laser fluence resulted in denser nanoparticle agglomeration distribution; this was noticed for higher nanoparticle diameters at higher laser fluences, where average nanoparticle diameters were found to be 36.9, 39.2, and 43.9 nm for fluences of 4.46, 5.73, and 7.01 J cm^{-2}, respectively, as shown in the insets of Fig. 2(d–f).

3.2 Fabricated device evaluation

Fig. 3(a) elucidates the current–voltage within the dark conditions, with the non-linear unsymmetric rectification

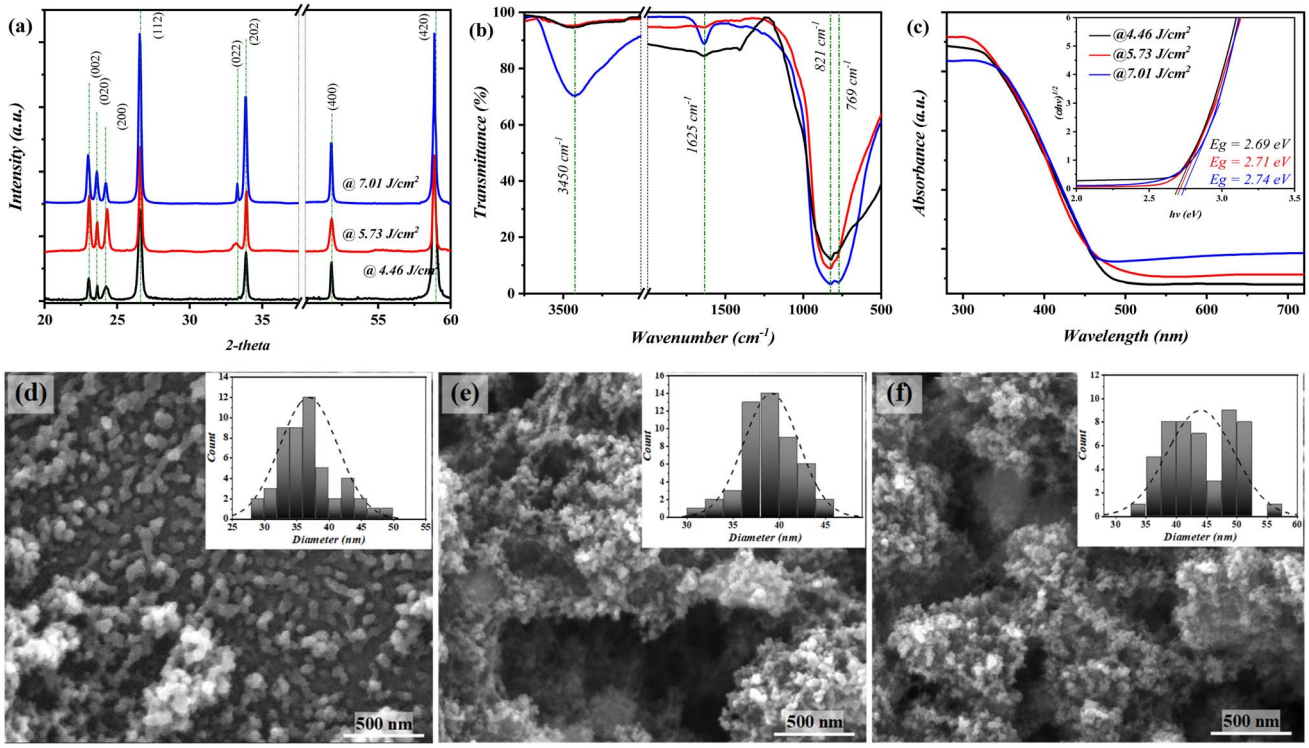

Fig. 2 The deposited WO_3 film characterization: (a) XRD, (b) FT-IR, (c) UV-Vis, and FE-SEM topographies for the fluences of (d) 4.46 J cm^{-2}, (e) 5.73 J cm^{-2}, and (f) 7.01 J cm^{-2}.

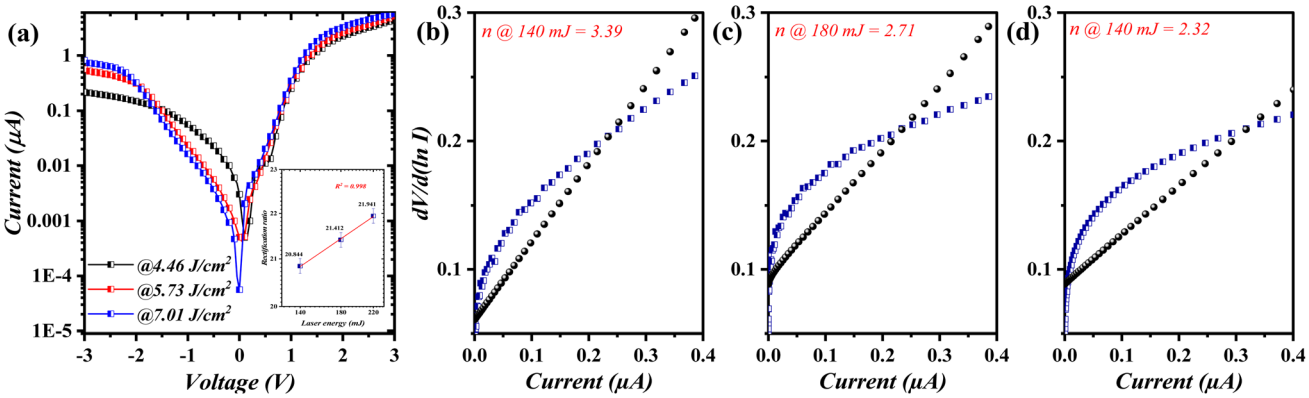

Fig. 3 (a) The dark current–voltage characteristics and dV/d(ln I) – I plots of the fabricated photodetectors for the fluences of (a) 4.46 J cm^{-2}, (b) 5.73 J cm^{-2}, and (c) 7.01 J cm^{-2}.

performances at the WO_3 and Si interface for all the proposed photodetectors. The attained knee bias was located at around ~0.9 V through current–voltage extrapolation. This was attained together with an augmented rectification ratio ($I_{forward}/I_{reverse}$, at ±3 V) going from 20.8 to 21.9 as a function of laser fluence, as shown in the inset of Fig. 3(a). The forward-region current–voltage curves show an exponential augmentation, which indicates the charge conduction mechanism through the so-called thermionic emission.[21] According to the well-defined ideal diode formula, the saturation current (I_s) is independent of the reverse voltage and only increases as the operation temperature increases due to minor thermal generation changes. However, in nonideal diode-like behavior, both lattice mismatch and thermal disturbance can be attained at the junction interface, resulting in the effect of electron tunneling between the VB of Si and CB of WO_3. The ideality factors (n) of the fabricated photodetectors were estimated from the forward current–voltage curve under dark conditions in accordance with Cheung's formula.[22,23] Herein, devices fabricated at laser fluences of 4.46, 5.73, and 7.01 J cm^{-2} exhibited n values of 3.39, 2.71, and 2.32, respectively, indicating higher/favorable diode-like behavior at higher laser fluence in the semiconductor framework. However, the attained n values (>2) indicated that the demonstrated forward dark current is not completely

governed by depletion-region and/or diffusion, yet significant contributions through the trap-limited conduction and interface-state aided tunneling within the deposited WO_3.[24,25]

Fig. 4(a–c) represent the fabricated photodetector characteristics as a function of wavelength, with a laser fluence of 7.01 J cm^{-2} under illumination with light of 15.3 μW cm^{-2}. In detail, the reverse bias current–voltage curves (Fig. 4(a)) demonstrate an increasing trend as a function of the applied illumination wavelength, which indicates a high diode-like performance under 460 nm, with respect to the scanned bias voltage. This behavior could be due to the inner potential-based absorbed photons; an internal electric field is acquired from the n- to p-side, which leads to the formation of built-in potentials; an electron–hole pair is formed, due to which a recombination photo-current is attained. The sensitivity profile/s, attained at −3 V applied bias, of the proposed photodetector, including I_{ph}/I_D, photo-responsivity ($R_\lambda = I_{ph} - I_D/P_{in}$, Fig. 4(b)), photo-detectivity ($D^* = R_\lambda \times A^{1/2}/(2qI_D)^{1/2}$), and external quantum efficiency (EQE = $[(I_{photo}/e)(P_{incident}/h\nu)]$, Fig. 4(c)), exhibited wavelength dependence.[26] In general, all addressed figures of merit revealed peak values at a wavelength of 460 nm; this corresponds to the attained optical bandgaps, as shown inset in Fig. 2(c). This could be mainly due to the photo-generated carriers at around 460 nm representing the absorption edge of the deposited WO_3 layer, which is the closest incident wavelength to the optical bandgap (absorption edge) of the active layer.

An I_{ph}/I_D ratio as high as 300% was attained under the influence of 460 nm with an R_λ value of 0.87 A W^{-1}; these values (300% and 0.87 A W^{-1}) were found to be lower at wavelengths lower or higher than 460 nm. However, an increased R_λ (0.55 A W^{-1}) was perceived at wavelengths higher than 700 nm, which is attributed to the window effect of the utilized Si wafer.[27,28] The $D^*$and EQE attained at 460 nm demonstrated similar trends to those in Fig. 4(b), with the highest values of 7.4 ×10^{11} Jones and 233%, respectively. The illumination power profile is presented in Fig. 4(d–f). In particular, a linear increase in the reverse current–voltage profile was observed as a function of the incident illumination power (Fig. 4(d)) and wavelength of 460 nm; the calculated LDR values revealed a positive linear correlation

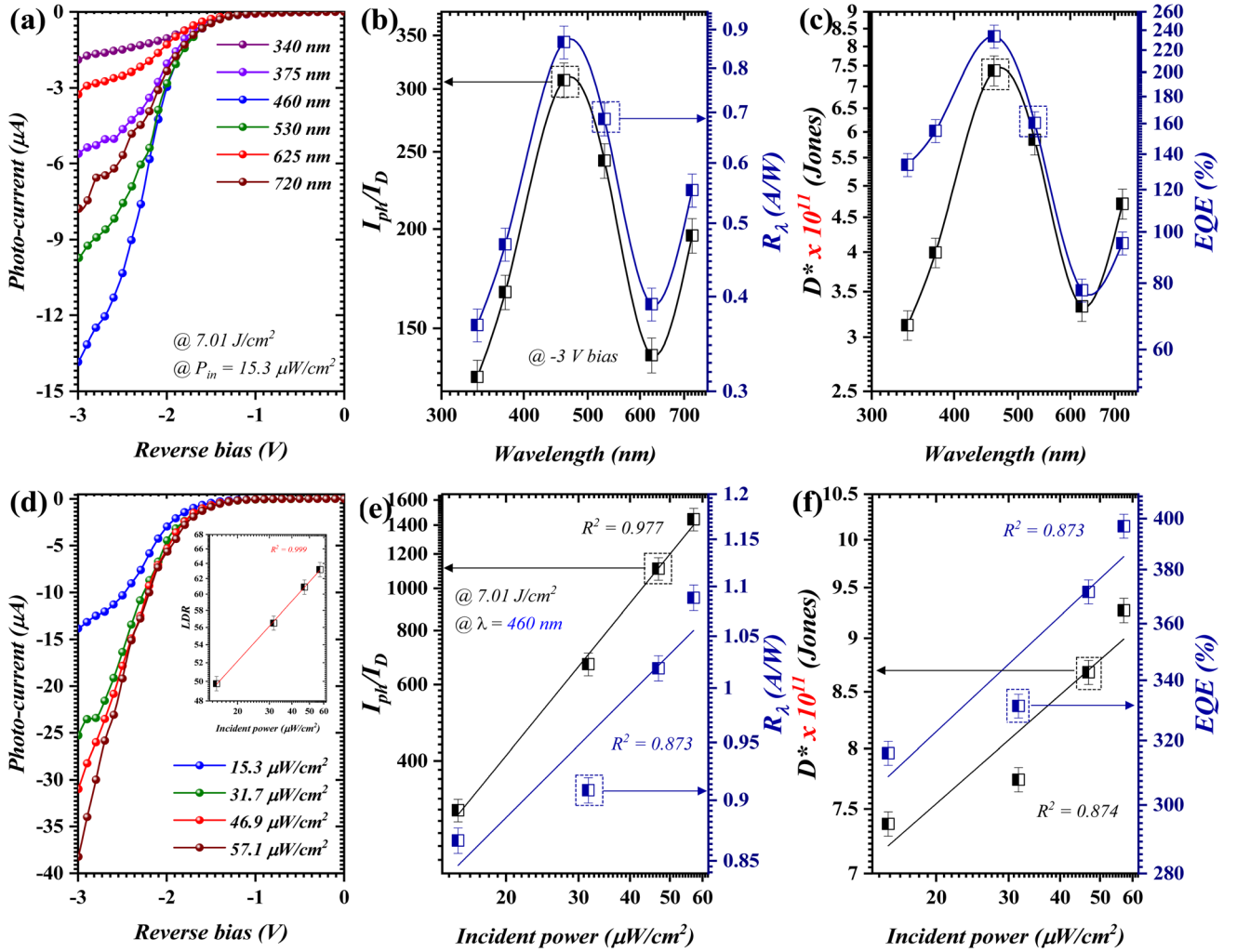

Fig. 4 The fabricated photodetector at a fluence of 7.01 J cm^{-2}. (a) Reverse bias I–V curve, (b) I_{ph}/I_D and R_λ, and (c) D^* and EQE as functions of incident wavelength. (d) Reverse bias I–V curve, (e) I_{ph}/I_D and R_λ, and (f) D^* and EQE as functions of incident power density.

to incident illumination from 15.3 to 57.1 μW cm^{-2} with an R^2 value of 0.999, as shown in the inset of Fig. 4(d). Similarly, the obtained figures of merit demonstrated increasing profile/s as a function of the incident illumination; this was perceived along with an average R^2 value close to unity. The R_λ, I_{ph}/I_D, D^*, and EQE exhibited values of 1.09 A W^{-1}, 1443%, 9.3 ×10^{11} Jones, and 397%, respectively, at an illumination of 57.1 μW cm^{-2}.

The dependency of both I_{ph} and R_λ on the incident optical power was evaluated *via* a power–law correlation (I_{ph}, $R_\lambda \propto P^\theta$). For the photodetector demonstrated in Fig. 4(d–f), I_{ph} exhibited a clear linear trend with an exponent of $\theta \approx 1.16$, which indicates the collection efficiency enhancement as a function of the increased incident photon ratio; this suggests the suppression of trap-assisted recombination and trap filling. In contrast, R_λ exhibited a relatively weak sub-linear scaling with an exponent of $\theta \approx 0.166$. The attained scaling (I_{ph} and R_λ) is consistent with the dynamics of defect-mediated carriers, where a higher ratio of incident photons reflects an enhanced charge separation, as well as saturated recombination centers.[29]

Fig. 5(a–c) illustrates the time-resolved characteristics of the fabricated photodetector under a fluence of 7.01 J cm^{-2}. The proposed device exhibited three multiple cycles of on/off states with acceptable stability over 15 seconds per cycle (Fig. 5(a)). The response/recovery times were found to be 163 and 172 ms, respectively, indicating the responsive profile of the WO_3/Si heterojunction photodetector, shown in the inset of Fig. 5(a). The presented device (at 7.01 J cm^{-2}) exhibited high stability as compared to other devices (4.46 and 5.73 J cm^{-2}). This could be because a higher laser fluence resulted in the denser formation of WO_3 particles, which resulted in a better quality of electron mobility;[30,31] this could be clearly perceived in the FE-SEM analysis. Long-term stability testing was also conducted (Fig. 5(b)) over a period of seven days, with a highly stable profile indicating the reproducible performance of the proposed geometry. Another stability profile was also conducted for nearly four minutes, as shown by the red lines in Fig. 5(b). The illumination power-dependent time-resolved characteristics are presented in Fig. 5(c); specifically, a linear increment of the tested device's photocurrent was found with an R^2 value of 0.993.

The suggested band alignment of the fabricated *n*-WO_3/p-Si heterostructure revealed the type-II configuration (Fig. 6); this plays a vital role in efficient photocarrier separation. Under dark conditions, the higher electron affinity and bandgap of the utilized p-Si result in the alignment of the Fermi level, which in turn forms a built-in electric field across the depletion region. Once illuminated, a photon that possesses higher energy as

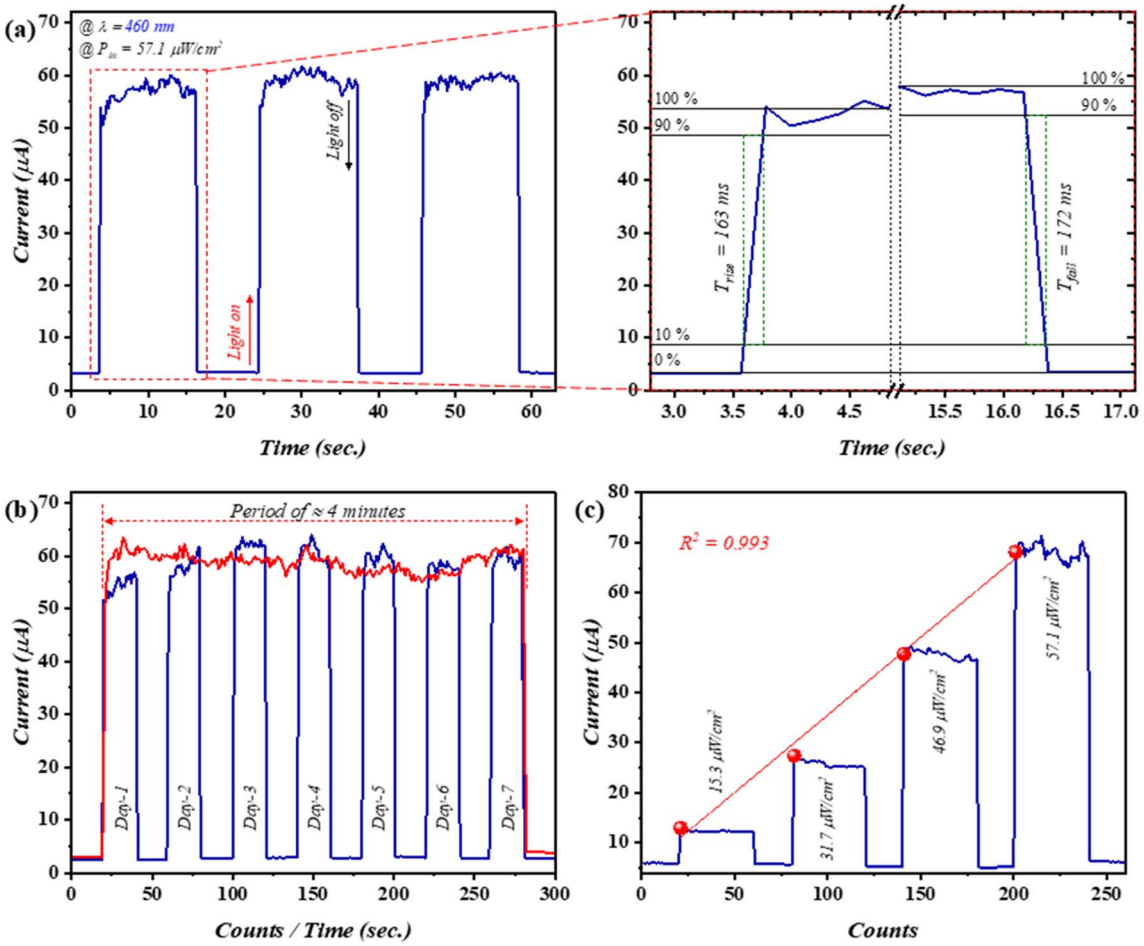

Fig. 5 The fabricated photodetector at a fluence of 7.01 J cm^{-2}. (a) Switching behavior, (b) long-term stability, and (c) power-dependent time-resolved characteristics.

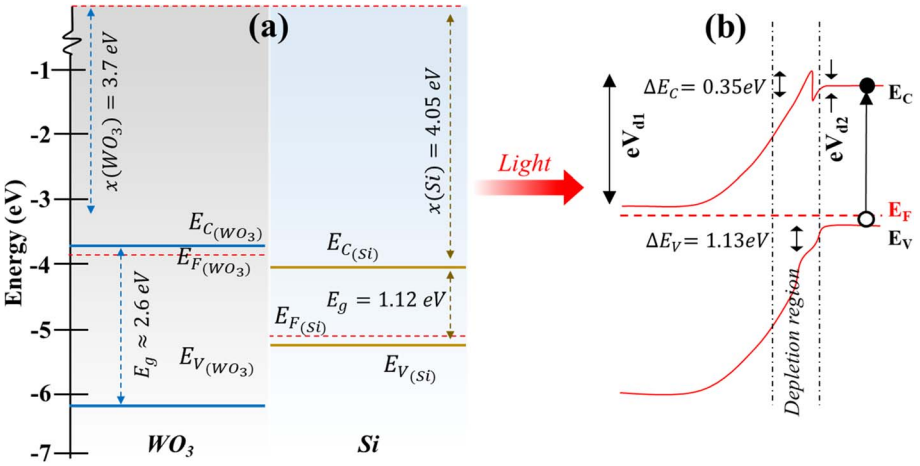

Fig. 6 Band alignment of the proposed *n*-WO_3/p-Si photodetector.

compared to the bandgap generates electron–hole pairs. In such a configuration, the *n*-WO_3's CB minimum resides at ~0.35 eV above the p-Si substrate, while the p-Si's VB maximum dwells ~1.1 eV above the *n*-WO_3's VB; this allows the arrangement of type-II offsets. In conjunction with the built-in electric field, molded after Fermi alignment, a driving force is provided for carrier separation. Photo-excited electrons are transferred from the CB of WO_3 downhill to that of the Si minimum, then pushed toward the external circuit *via* the generated electric field, while the obtained holes are transferred from the Si VB to that of WO_3.[32–34]

4. Conclusion

Visible light n-type WO_3/p-type Si photodetector/s were successfully fabricated as a function of laser fluence *via* the PLD technique. The microstructural features exhibited a bandgap value of 2.6 eV, with the nanoparticle diameter profile increasing from 36.9 to 43.9 nm for fluences of 4.46 and 7.01 J cm^{-2}, respectively. The R_λ profile indicated both illumination power and incident wavelength dependencies, where values of 0.87 and 1.09 A W^{-1} were perceived under illumination of 15.3 and 57.1 μW cm^{-2} at 460 nm incident wavelength, with an average R^2 value of 0.899. Concurrently, figures of merit, including R_λ, D^*, and EQE, revealed relatively lower values at wavelengths higher/lower than 460 nm. However, augmented profiles were noticed at wavelengths ≥ 700 nm due to the window effect of the utilized Si wafer. The time-resolved characteristics indicate a steady photodetector performance with response/recovery times of 163 and 172 ms, respectively.

Conflicts of interest

There are no conflicts to declare.

Data availability

All data used in this study are presented in the main manuscript.

References

1 E. T. Salim, *et al*, The unclad single-mode fiber-optic sensor simulation for localized surface plasmon resonance sensing based on silver nanoparticles embedded coating, *Plasmonics*, 2024, **19**(1), 131–143.
2 Z. Yang, *et al*, Ultra-sensitive self-powered WSe 2/Si vdW photodiode enabling high-precision non-invasive pulse oximetry monitoring, *Nano Res.*, 2025, **18**(6), 94907477.
3 D. Wu, *et al*, Integrated mid-infrared sensing and ultrashort lasers based on wafer-level Td-WTe2 Weyl semimetal, *Appl. Phys. Rev.*, 2024, **11**(4), DOI: **10.1063/5.0204248**.
4 X. Li, *et al*, Van der Waals hybrid integration of 2D semimetals for broadband photodetection, *Adv. Mater.*, 2025, 2415717.
5 W. Wu, *et al*, Vertical integrated PtSe2/4H-SiC vdW heterojunction for ultra-sensitive UV imaging and flame detection, *Opt. Lett.*, 2025, **50**(13), 4362–4365.
6 N. Z. Abed, R. A. Ismail and S. S. Shaker, Role of substrate temperature on the performance of BaTiO3/Si photodetector prepared by pulsed laser deposition, *Sci. Rep.*, 2024, **14**(1), 4531.
7 R. A. Ismail, A. M. Mousa and S. S. Shaker, Visible-enhanced silver-doped PbI2 nanostructure/Si heterojunction photodetector: effect of doping concentration on photodetector parameters, *Opt. Quantum Electron.*, 2019, **51**(11), 362.
8 E. Y. Salih, Fabrication and photodetection performance evaluation of nanostructured CdS/Si MSM visible light photodetector, *Opt. Mater.*, 2024, **149**, 115120.
9 E. Y. Salih, Fabrication of CdSe/Si nanostructure for self-powered visible light photodetector, *Mater. Lett.*, 2024, **371**, 136930.
10 B. R. Kumar, *et al*, Enhancing the properties of CdO thin films by co-doping with Mn and Fe for photodetector applications, *Sens. Actuators, A*, 2021, **319**, 112544.
11 S. Bansal, *et al*, Bilayer graphene/HgCdTe based very long infrared photodetector with superior external quantum

efficiency, responsivity, and detectivity, *RSC Adv.*, 2018, **8**(69), 39579–39592.
12 M. F. Jawad, R. A. Ismail and K. Z. Yahea, Preparation of nanocrystalline Cu2O thin film by pulsed laser deposition, *J. Mater. Sci.: Mater. Electron.*, 2011, **22**(9), 1244–1247.
13 A. M. M. Ali, *et al*, Nanostructured visible-enhanced CdS/SiO2/Si heterojunction photodetectors: synthesis, characterization, and performance optimization, *Physica B: Condensed Matter*, 2023, **669**, 415303.
14 M. A. Jabr, A. M. Ali and R. A. Ismail, Preparation of high-performance p-CuO/n-Si heterojunction photodetector by laser-assisted chemical bath deposition: effect of laser wavelength, *Ceram. Int.*, 2023, **49**(7), 11442–11451.
15 P. Dong, *et al*, Highly enhanced photocatalytic activity of WO 3 thin films loaded with Pt–Ag bimetallic alloy nanoparticles, *RSC Adv.*, 2017, **7**(2), 947–956.
16 V. Pasindu, *et al*, Multifunctional transition metal oxide/graphene oxide nanocomposites for catalytic dye degradation, renewable energy, and energy storage applications, *RSC Adv.*, 2025, **15**(40), 33162.
17 Z. Yan, *et al*, A cost-effective Co3O4@ WO3 hetero-structure derived from WO3@ Co-CoPBA for oxygen evolution reaction, *RSC Adv.*, 2025, **15**(36), 29925.
18 Y. W. Jo, *et al*, Fabrication of Ag 2 O/WO 3 p–n heterojunction composite thin films by magnetron sputtering for visible light photocatalysis, *RSC Adv.*, 2020, **10**(27), 16187–16195.
19 A. A. Najim, S. S. Shaker and M. A. Muhi, Room temperature NO2 gas sensor based on SnO2-WO3 thin films, *Plasmonics*, 2017, **12**(4), 1051–1055.
20 P. J. Boruah, R. R. Khanikar and H. Bailung, Synthesis and characterization of oxygen vacancy induced narrow bandgap tungsten oxide (WO3−x) nanoparticles by plasma discharge in liquid and its photocatalytic activity, *Plasma Chem. Plasma Process.*, 2020, **40**(4), 1019–1036.
21 X. Zhang, *et al*, The mechanism of performance variations in MoS 2 vertical Schottky metal–semiconductor photodiode based on thermionic emission theory, *IEEE Trans. Electron Devices*, 2022, **69**(10), 5644–5648.
22 S. Cheung and N. Cheung, Extraction of Schottky diode parameters from forward current-voltage characteristics, *Appl. Phys. Lett.*, 1986, **49**(2), 85–87.
23 A. Kocyigit, *et al*, Investigation of AlN-based Schottky type photodetector in visible light detection, *Phys. B*, 2024, **690**, 416286.
24 M. Raja, *et al*, Impact of annealing treatment on structural and dc electrical properties of spin coated tungsten trioxide thin films for Si/WO3/Ag junction diode, *Mater. Sci. Semicond. Process.*, 2016, **56**, 145–154.
25 A. Danilyuk, *et al*, An enhanced charge carrier separation in a heterojunction solar cell with a metal oxide, *Phys. Status Solidi A*, 2022, **219**(1), 2100525.
26 S. Chen, *et al*, Two-dimensional GeS/SnSe2 tunneling photodiode with bidirectional photoresponse and high polarization sensitivity, *ACS Appl. Mater. Interfaces*, 2024, **16**(26), 33740–33751.
27 M. B. A. Bashir, *et al*, The impact of laser energy on the photoresponsive characteristics of CdO/Si visible light photodetector, *J. Micromech. Microeng.*, 2022, **32**(8), 085006.
28 X. Liu, *et al*, Infrared photodetector based on the photothermionic effect of graphene-nanowall/silicon heterojunction, *ACS Appl. Mater. Interfaces*, 2019, **11**(19), 17663–17669.
29 J. Ma, *et al*, 2D Double Heterostructure Infrared Photodetector with Type-III Band Alignment by Incorporating Bi2Se3 Layer, *Adv. Opt. Mater.*, 2024, **12**(12), 2302563.
30 E. Y. Salih, *et al*, Rapid fabrication of NiO/porous Si film for ultra-violate photodetector: The effect of laser energy, *Microelectron. Eng.*, 2022, **258**, 111758.
31 Y. Yao, *et al*, A review on the properties and applications of WO3 nanostructure-based optical and electronic devices, *Nanomaterials*, 2021, **11**(8), 2136.
32 F. Sanchez, *et al*, WO3 work function enhancement induced by filamentous films deposited by resistive heating evaporation technique, *J. Alloys Compd.*, 2023, **968**, 171888.
33 F. Wang, C. Di Valentin and G. Pacchioni, Electronic and structural properties of WO3: a systematic hybrid DFT study, *J. Phys. Chem. C*, 2011, **115**(16), 8345–8353.
34 J. Zhu, *et al*, Intrinsic defects and H doping in WO3, *Sci. Rep.*, 2017, **7**(1), 40882.